Nanoscale

Self-Assembled Vertically Aligned Ni Nanopillars in CeO2 with Anisotropic Magnetic and Transport Properties for Energy Applications

Journal:	*Nanoscale*
Manuscript ID	NR-ART-07-2018-005532.R1
Article Type:	Paper
Date Submitted by the Author:	14-Aug-2018
Complete List of Authors:	Huang, Jijie; Purdue University, Materials Engineering; Qi, Zhimin; Purdue University System Li, Leigang; Purdue University Wang, Han; Purdue University Xue, Sichuang; Purdue University Zhang, Bruce; Purdue University Zhang, Xinghang; Purdue University System Wang, Haiyan; Purdue University System, MSE; Neil Armstrong Engineering Building

SCHOLARONE™
Manuscripts

Nanoscale

Self-Assembled Vertically Aligned Ni Nanopillars in CeO$_2$ with Anisotropic Magnetic and Transport Properties for Energy Applications

Jijie Huang[a], Zhimin Qi[a], Leigang Li[a], Han Wang[a], Sichuang Xue[a], Bruce Zhang[b], Xinghang Zhang[a] and Haiyan Wang *[a, b]

Self-assembled vertically aligned metal-oxide (Ni-CeO$_2$) nanocomposite thin films with novel multifunctionalities have been successfully deposited by a one-step growth method. The novel nanocomposite structures present high density Ni-nanopillars vertically aligned in CeO$_2$ matrix. Strong and anisotropic magnetic property has been demonstrated, with a saturation magnetization (M$_s$) of ~175 emu/cm^3 and ~135 emu/cm^3 for out-of-plane and in-plane directions, respectively. Such unique vertically aligned ferromagnetic Ni nanopillars in CeO$_2$ matrix have been successfully incorporated in high temperature superconductor YBa$_2$Cu$_3$O$_7$ (YBCO) coated conductors as effective magnetic flux pinning centers. The highly anisotropic nanostructures with high density vertical interfaces between the Ni nanopillars and CeO$_2$ matrix also promote the mixed electrical and ionic conductivity out-of-plane and thus demonstrate great potentials as nanocomposite anode materials for solid oxide fuel cells and other potential applications requiring anisotropic ionic transport properties.

Introduction

Multifunctional two-phase vertically aligned nanocomposite (VAN) provides great opportunity to achieve extraordinary properties arising from the two phases and their highly strained vertical heterointerfaces.[1-3] The design potentials of VAN systems towards desirable properties are enormous, given the large selection of materials and the two-phase combinations. Most of the VAN demonstrations are oxide-oxide systems with the goals of either enhanced physical properties or combined functionalities through the two-phase coupling. For example, tunable band structure,[4] vertically exchange bias,[5] multiferroics,[6] magnetoresistance,[7, 8] novel anisotropic electronic-ionic transport,[9, 10] and coupled extraordinary dielectric and optical performance,[11, 12] have been demonstrated in various oxide-oxide VAN systems. The growth mechanisms for different 2-phase oxide-oxide systems have also been explored,[1] which are correlated with various morphologies observed, including nanocheckerboard structures,[11, 13] nanopillars in matrix,[14, 15] and 2-phase domain structures.[16]

Very different from the oxide-oxide VAN systems, the metal-oxide VAN systems with vertically aligned metal nanopillars embedded in oxide matrix provide another large group of materials selection (i.e., metals) and novel functionalities in the VAN designs. For example, the metal-oxide nanocomposite systems are considered as hybrid metamaterials for novel plasmonic and optical properties. Currently, electrochemical deposition into a porous alumina template[17, 18] and complicated nanofabrication approaches such as combined focus ion beam (FIB) and electroplating,[19] electron beam lithography,[20] and electron beam evaporation,[21] are mostly involved to synthesis such metal-oxide hybrid materials. The costly template and tedious nanofabrication methods limit the further scale-up processing for applications, in addition, it is challenging to obtain ultra-fine metal pillars (≤10 nm) by these methods. To overcome these challenges, a one-step PLD method has been demonstrated to grow self-assembled metal-oxide VAN systems with high epitaxial quality.[22, 23] For example, Co-BaZrO$_3$ (BZO) nanocomposite thin films have been deposited with Co nanopillars embedded in BZO matrix, and the pillar size can be tailored by changing deposition frequency.[22] Some of the metal-oxide nanocomposites were also later realized by a magnetron sputtering technique.[24] Compared to the relatively easy growth of oxide-oxide VAN, challenges emerge to achieve metal-oxide VAN, due to the completely different growth kinetics for metals and oxides, as well as different surface energy and wetting properties on substrates, and possible inter-diffusion.

[a.] School of Materials Engineering, Purdue University, West Lafayette, IN, 47906 USA
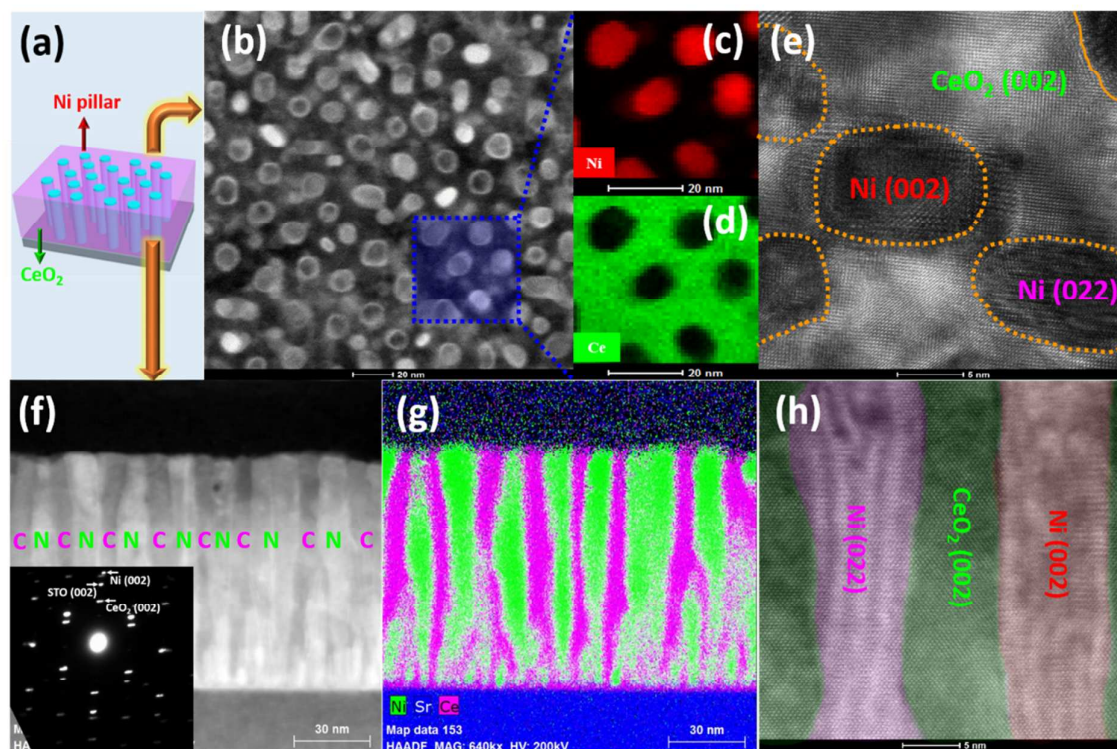[b.] School of Electrical and Computer Engineering, Purdue University, West Lafayette, IN, 47906 USA

Figure 1 Microstructure study of Ni-CeO₂ film deposited on STO substrate. (a) 3D schematic illustration of the film; (b) Plan-view STEM image of a selected area of the film, with EDS mapping of (c) Ni and (d) Ce elements; (e) high resolution image to show the crystal structure of the pillars; (f) Cross-sectional STEM image of a selected area of the film with selected area electron diffraction (SAED) pattern and (f) its corresponding EDS mapping; (h) Atomic-scale high resolution STEM image of a selected area with Ni pillars.

To overcome these challenges, careful materials selection and growth condition optimization are essential. In this study, we selected a face-centered (fcc) cubic metal, Ni and a cubic (fluorite) oxide, CeO₂, as the two phases. The expected structure is illustrated in Fig. 1a, exhibiting a VAN structure of Ni nanopillars embedded in CeO₂ matrix. The interests for this metal-oxide system include the anisotropic magnetic Ni nanopillars, as well as the anisotropic ionic and electrical conductivity of Ni-CeO₂ nanocomposites. Take the advantage of the anisotropy nature of the magnetic Ni nanopillars, various applications are envisioned, such as high-density magnetic recording media and nanoscale magnetic flux pinning centers for high temperature superconducting thin films. For example, in terms of magnetic flux pinning properties, the magnetic Ni nanopillars in this case are expected to provide magnetic pinning effect for superconducting YBa₂Cu₃O₁₋ₓ (YBCO) thin film, and CeO₂ matrix can effectively encapsulate Ni and minimize the possible inter-diffusion between the metal Ni and YBCO layer. [25-29] In this work, the Ni-CeO₂ nanolayer is introduced into YBCO as cap layer to investigate its pinning effect. Furthermore, by including the conducting Ni metal pillars, the overall vertical conductivity of the film is enhanced and thus a highly anisotropic conductor is designed and demonstrated.

Results and discussion

A typical plan-view scanning transmission electron microscopy (STEM) image shown in Fig. 1b well captures the obvious Ni nanopillars with an average diameter of ~7 nm. Energy-

dispersive X-ray spectra (EDS) mapping of selected area was conducted to determine the two phases, Ni (Ni elemental mapping in Fig. 1c) and CeO₂ (Ce elemental mapping in Fig. 1d). The sharp interface between them suggests that there is very little or no intermixing between the metal and oxide phases in the nanocomposite film. In addition, the volume ratio of Ni nanopillars can be estimated to be ~55% based on multiple plan-view STEM images. Both Ni (002) and Ni (022) nanopillars can be identified in the high-resolution TEM image in Fig. 1e, as Ni (a=3.524 Å) is not perfectly matched with STO substrate (a=3.905 Å) and thus presents two possible orientations. Cross-sectional STEM was then carried out to explore the 3-D nature of the composite film. It is obvious that the vertically self-assembled Ni nanopillars were grown throughout the entire thickness of the film, as shown in the low-mag STEM image in Fig. 1f. Corresponding EDS mapping in Fig. 1g shows clear Ni nanopillars in CeO₂ matrix with clean out-of-plane interface. Furthermore, the surface of the film is relatively smooth, which can be further confirmed by the AFM image shown in Fig. S4 with a low surface roughness of R_q=1.33 nm. Fig. 1h displays high-resolution STEM image for a representative area with both Ni (002) and Ni (022) nanopillars, which further confirms the high film quality and no inter-mixing between Ni and CeO₂. It is also noted that the number of Ni (002) nanopillars is much larger than that of Ni (022) nanopillars. In addition, the ratio of Ni (002) and Ni (022) can be varied by controlling the growth condition. A higher

　　　　　　　　　　　　　　　　　　　　　　　　　　　　　　COMMUNICATION

growth temperature of 750 °C results in more Ni (022) pillars

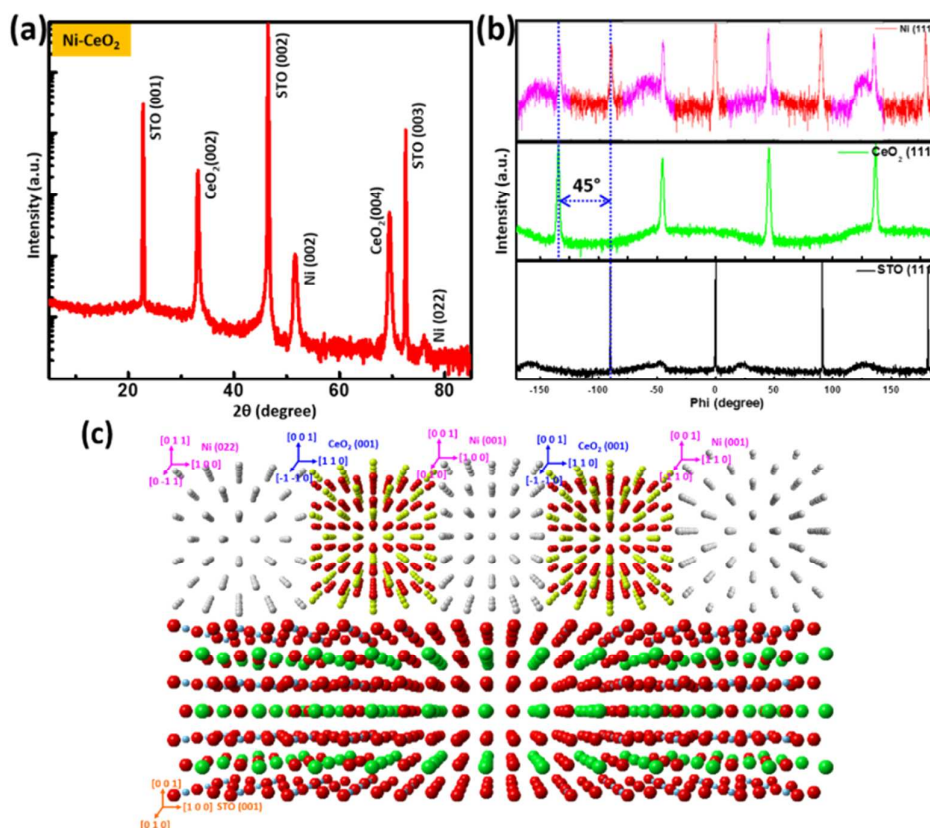(LME) growth. For the out-of-plane matching between CeO_2

Figure 2 (a) XRD θ-2θ pattern of Ni-CeO2 thin film grown on STO (001); (b) φ scan of STO (111), CeO₂ (111) and Ni (111) peaks; (c) crystallographic image to show the nanocomposite film built-up.

as revealed in Fig. S3 in the supporting information.

To examine the crystal structure and determine the phases in this metal-oxide composite thin film, X-ray diffraction (XRD) analysis was conducted. CeO_2 has grown preferably in the (00l)-direction, as demonstrated by the standard θ-2θ XRD pattern in Fig. 2a. Consistent with the above TEM/STEM analysis, Ni nanopillars grow preferably along the (002) orientation (2θ=51.637°) with some minor ones (022) orientation (2θ=76.095°), evidenced from the Ni peak intensities. Tensile strain along (002) and (022) for Ni (002) and Ni (022) can be determined, compared to bulk Ni from PDF #04-0850, which might enhance the magnetic response of Ni.[30] As mentioned, Ni presents a face-centered cubic (fcc) structure with a lattice parameter of a_{Ni}=3.524 Å, while the substrate STO has perovskite structure with a lattice constant of a_{STO}=3.905 Å. The lattice mismatch between Ni and STO is relatively high of 10.37% (calculated based on $f = (a_{STO} - a_{Ni})/(\frac{a_{STO}+a_{Ni}}{2})$). Thus, an in-plane domain matching epitaxy (DME) is applied to satisfy the epitaxial growth of Ni on STO,[31] i.e., 10 of $(002)_{Ni}$ match with 9 of $(002)_{STO}$. On the other hand, CeO_2 (a_{CeO2}=5.41134 Å) has a perfect lattice matching with STO after 45° rotation, which allows the lattice matching epitaxial

and Ni, DME is implemented for both Ni (002) and Ni (022), because of the large lattice mismatch in both cases. As the surface energy of Ni (002) is lower than that of Ni (022), more Ni is anticipated to grow along the c-direction, which is evidenced from the stronger Ni (00l) peaks in the XRD scans. Furthermore, the φ-scans of Ni (111), CeO_2 (111) and STO (111) are shown in Fig. 2b to explore the in-plane matching of the film with the substrate. Interestingly, Ni (111) scan shows a 8-fold pattern, which suggests the presence of two sets structural domains inside Ni (002). Therefore, two in-plane epitaxial relationship can be identified, Ni [100]//STO [100], Ni [010]//STO [010] and Ni [110]//STO [100], Ni [$\bar{1}$10]//STO [010]. In addition, for the Ni (022) domains, the in-plane matching with the substrate follows Ni [100]//STO [100] and Ni [0$\bar{1}$1]//STO [010]. Furthermore, CeO_2 (111) peaks exhibit an excellent match with STO (111) peaks after a 45° rotation. Based on the XRD results, the overall growth relationships of the Ni-CeO_2 nanocomposite film and STO substrate are determined and illustrated by the atomic crystallographic images in Fig. 2c.

The epitaxial growth of the metal-oxide nanocomposite thin film with self-assembled Ni nanopillars in CeO_2 matrix is
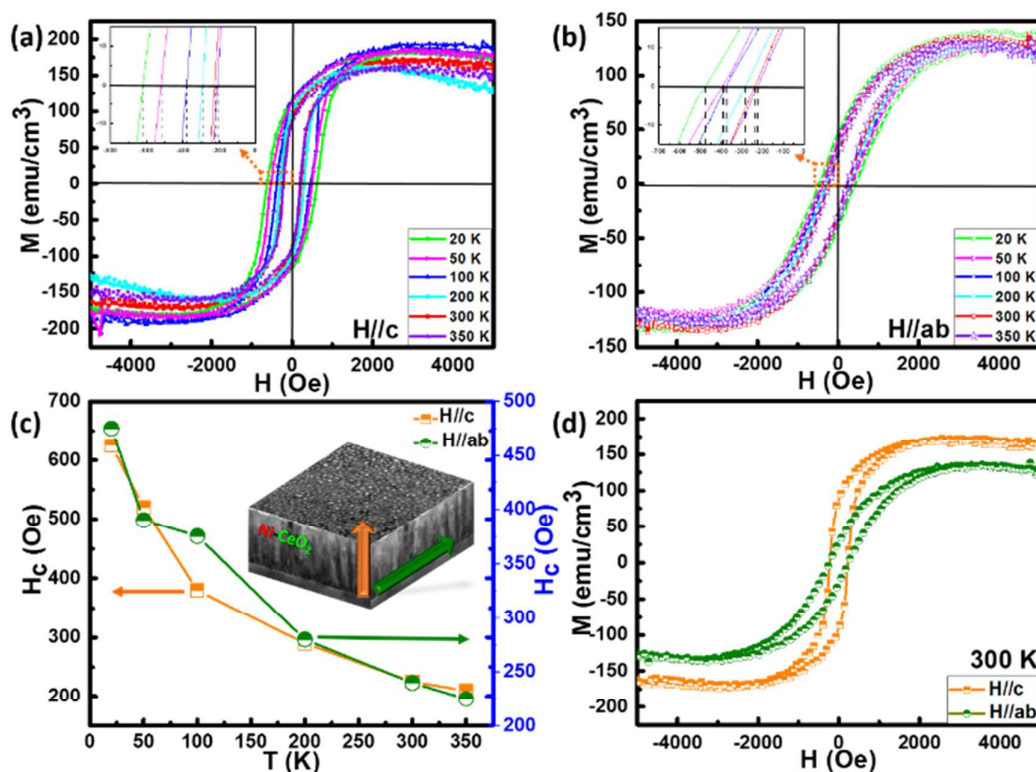
Figure 3 The magnetic hysteresis loops for the Ni-CeO$_2$ film at varying temperatures with applied magnetic field (a) parallel or (b) perpendicular to the film surface, and the insets are the enlargement of the marked area to identify coercivity values; (c) Coercivity values as function of the measured temperature; (d) In-plane and out-of-plane M-H curve comparison of the sample at room temperature to show its anisotropic magnetic performance.

quite interesting and thus worth further investigation. Similar to the intensively studied oxide-oxide VAN systems,[1-3] the growth mechanism of this metal-ceramic nanocomposite film follows two steps of nucleation and film growth. The surface energy for Ni (001), Ni (022), CeO$_2$ (001) and STO (001) is 2.426 J/m^2, 2.368 J/m^2, 1.0-1.4 J/m^2, and 1.26 J/m^2, respectively.[32-34] As a result, the higher interfacial energy (lower wettability) between Ni and STO (γ_{NS}) leads to the Volmer-Weber 3D island growth mode, which initiates 3D Ni islands nucleation and forms nanopillars finally. However, for the growth of CeO$_2$, either the 2D Frank-van der Merve mode or the 2D+3D Stranski-Krastanov mode is dominated because of its lower interfacial energy γ_{CS} (higher wettability) with STO, which results a layer-by-layer growth to form the overall matrix. The corporative growth of Ni and CeO$_2$ following their independent growth modes allows the formation of such metal-oxide VAN structure with Ni nanopillars embedded in CeO$_2$ matrix. This one-step PLD method can also be applied to many other metal-oxide systems, for example, an epitaxial Ni-BaTiO$_3$ (BTO) system has also been successfully grown, as presented of the microstructure characterizations in Fig. S1.

Nanostructured magnetic materials are promising for various technological applications, such as magnetic data storage. Taking the advantage of this self-assembled vertical Ni nanopillars, it is essential to explore the magnetic property of

these high density anisotropic nanopillars. The M-H measurement at different temperatures were carried out for Ni-CeO$_2$ nanocomposite films, and the hysteresis loops are shown in Fig. 3a for in-plane (IP: applied magnetic field parallel to film surface) and Fig. 3b for out-of-plane (OP: applied magnetic field perpendicular to film surface), respectively. The inserted figures are the enlarged area of the orange squares, which can be used to determine its coercivity (H$_c$) at different temperatures. As seen from the H$_c$ vs. temperature plot in Fig. 3c, the H$_c$ value decreases with increasing temperature, along both IP and OP directions, which suggests a thermally activated magnetization reversal process, as well as the existence of magnetic anisotropy of Ni-CeO$_2$ nanocomposite film. As the temperature increases, thermal fluctuations or thermal perturbations could reduce the coercivity, which has been observed in various other magnetic materials.[35, 36] The magnetic anisotropy can be clearly revealed by the M-H curves (at 300 K) comparing IP and OP measurements as shown in Fig. 3d. The saturation magnetization (M$_s$) is ~175 emu/cm^3 and ~135 emu/cm^3 for OP and IP, respectively. It is worth noting that the entire nanocomposite volume (including both the Ni nanopillars and the CeO$_2$ matrix) is taken into account. If considering the actual volume density of the magnetic Ni nanopillars in the overall film (~55%), its M$_s$ value can be as high as ~320 emu/cm^3 for OP and ~245 emu/cm^3 for IP. The M$_s$
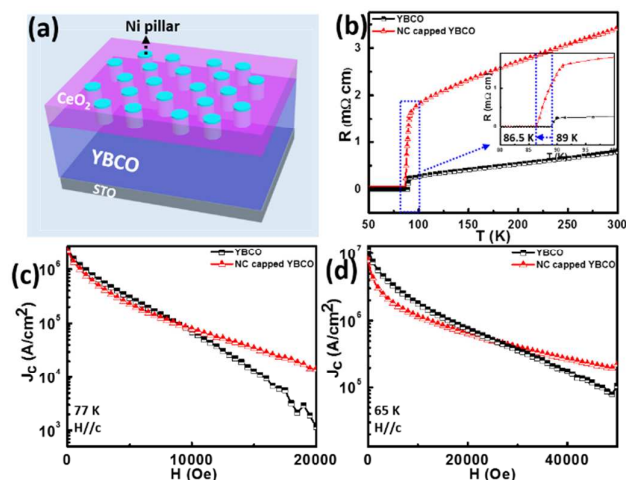
Figure 4 (a) Schematic illustration of the nanocomposite capped YBCO film; (b) R-T plots of YBCO thin films, with or without Ni-CeO$_2$ nanocomposite layer, inserted figure is the enlargement around the transition temperature regime; The in-field critical current density dependence of applied magnetic field for both films at (c) 77 K and (d) 65 K.

values are lower than that of 420 emu/cm^3 for bulk Ni,[37] which is possibly due to the very fine Ni nanopillars and the orientations of the Ni nanopillars ([001] and [022]) which are not along the easy axis of Ni [111]. It is noted that the field applied might not be strong enough to align all the magnetic dipoles in the hard magnetization direction. In this case, the magnetic anisotropy of the Ni nanopillars can be considered to be from the competition between magneto-crystalline anisotropy and shape anisotropy, if the interaction between the Ni nanopillars is ignored. As the growth directions of the Ni nanopillars are [001] and [022] in this case, there is an angle of 54.73° and 35.27° with the magneto-crystalline easy axis of [111]. Therefore, the shape anisotropy is considered as the dominated factor for the magnetic anisotropy in Ni nanopillars. In addition, the temperature-dependence of magnetization of Ni-CeO$_2$ was measured up to 380 K (due to the limitation of the PPMS tool) with an applied magnetic field perpendicular to the film surface, as shown in Fig. S2. As shown, the magnetization does not disappear up to 380 K, which is because that the Curie temperature of Ni is 627 K.

As mentioned above, magnetic nanostructures could provide magnetic flux pinning effect for high temperature superconductors to achieve better in-field superconducting properties (especially the in-field critical current density $J_c^{in-field}$). Therefore, this nanocomposite thin film with high-density magnetic Ni nanopillars could be an ideal candidate for magnetic pinning effect. As a demonstration, a thin layer of the Ni-CeO$_2$ VAN was incorporated into YBCO for flux pinning enhancement, as illustrated in the schematic drawing in Fig. 4a. The magnetic Ni nanopillars act as effective magnetic flux pinning centers, while the CeO$_2$ matrix effectively encapsulates the Ni nanopillars and minimizes the inter-diffusion between the YBCO and Ni. The microstructure study in Fig. S5 confirms that no or very limited inter-diffusion exists between the YBCO

layer and Ni-CeO$_2$ layer on top. Superconducting properties (e.g., transition temperature T_c and critical current density J_c) are measured for YBCO thin films, with or without the Ni-CeO$_2$ nanocomposite layer. First, the R-T property was measured and plotted in Fig. 4b. The inserted plot is the enlarged transition regime to determine the T_c values. The results show that the temperature where the resistivity goes to absolute zero (T_c^{zero}), is 86.5 K for the doped YBCO and 89 K for pure YBCO, respectively, which is comparable to previous reports.[26-29, 38, 39] The slightly T_c drop of the YBCO with Ni-CeO$_2$ layer might be resulted from the incorporation of the Ni-CeO$_2$ nanocomposite layer. More importantly, the J_c values were also measured and compared at 77 K (Fig. 4c) and 65 K (Fig. 4d), with the applied magnetic field perpendicular to the film surface (H//c). Under the low applied field, the J_c value of pure YBCO is higher, while the J_c-H curve becomes flatter for Ni-CeO$_2$ (NC) capped YBCO with increasing field. And, the absolute value of J_c of Ni-CeO$_2$-capped YBCO exceeds pure YBCO at higher fields beyond 1T and 2.5T, for 77K and 65K, respectively. This suggests that the magnetic pinning is effectively introduced by the Ni-CeO$_2$ nanocomposite in the high field regime. The results demonstrate the effective pinning enhancement by Ni-CeO$_2$ nanocomposite, especially at high fields, which indicates the potential high field applications of YBCO with Ni-CeO$_2$ nanocomposite. In such scheme, a magnetic pinning force is generated by the interaction between the magnetic Ni nanopillars and the magnetic flux in vortices of YBCO, which accordingly requires larger Lorentz force to move the normal cores. Therefore, magnetic pinning is provided by the magnetic Ni nanopillars.

To explore the anisotropic transport property of this unique Ni-CeO$_2$ nanocomposite thin film, AC impedance measurement was carried out, in both IP and OP directions. The EIS data in Fig. S6 of both OP and IP directions proves the incorporation of Ni metal in the CeO$_2$ matrix greatly reduce the resistance compared to pure CeO$_2$. The IP data for both Ni-CeO$_2$ and pure CeO$_2$ is shown in Fig. S6a, and the Ni-CeO$_2$ nanocomposite presents a much smaller semicircle than that of the pure CeO$_2$. Both CeO$_2$ films, with or without Ni nanopillars, show a similar single semi-circle characteristic instead of two semi-circles as seen in the cases of bulk materials, which is believed to be caused by the large stray capacitance from the substrate.[38] For the OP measurement in Fig. S6b, the Ni-CeO$_2$ composite shows the behavior of an inductor because of the highly conductive nature since metallic Ni is vertically aligned throughout the entire film and becomes the preferred conduction paths. Besides, the second component in the low frequency regime represents the electrode effect.[40] The incomplete semi-circle at high frequency regime is due to the limitation of impedance analyser used. Overall, the unique Ni-CeO$_2$ vertically aligned nanocomposite film presents a highly anisotropic transport property.

Conclusions

The self-assembled Ni-CeO$_2$ nanocomposite thin films have been successfully grown by a one-step PLD method, with carefully controlled growth conditions. From the microstructure study, high density ultra-fine Ni nanopillars of ~7 nm embedded in the CeO$_2$ matrix has been successfully demonstrated. High epitaxial quality of both phases has been demonstrated with a sharp interface. The metal-oxide nanocomposite films with anisotropy magnetic property (i.e., the preferred OP magnetization) has been incorporated into superconducting YBCO thin film as a cap layer. Enhanced flux pinning properties in the doped YBCO film have been demonstrated compared to pure YBCO thin films, especially in the high magnetic field regime. Highly anisotropic electrical and ionic conductivity in Ni-CeO$_2$ nanocomposite thin films could be ideal for thin film anode structure in SOFCs. This unique anisotropic metal-oxide nanocomposite thin film could find promising applications in high-density magnetic data storage and magnetic tunnel junction devices.

Conflicts of interest

There are no conflicts to declare.

Acknowledgement

References

1   1 J. L. MacManus-Driscoll, *Adv. Funct. Mater.*, 2010, **20**, 2035-2045.
2   H. Y. Hwang, Y. Iwasa, M. Kawasaki, B. Keimer, N. Nagaosa and Y. Tokura, *Nat. Mater.*, 2012, **11**, 103.
3   J. Huang, J. L. MacManus-Driscoll and H. Wang, *J. Mater. Res.*, 2017, **32 (21)**, 4054.
4   W. Chang, H. Liu, V. Tra, J. Chen, T. Wei, W. Y. Tzeng, Y. Zhu, H. Kuo, Y. Hsieh, J. Lin, Q. Zhan, C. Luo, J. Lin, J. He, C. Wu and Y. Chu, *ACS Nano*, 2014, **8(6)**, 6424-6429.
5   J. Huang, A. Gellatly, A. Kauffmann, X. Sun and H. Wang, *Cryst. Growth Des.*, 2018, **18**, 4388-4394.
6   H. Zheng, J. Wang, S. E. Lofland, Z. Ma, L. Mohaddes-Ardabili, T. Zhao, L. Salamanca-Riba, S. R. Shinde, S. B. Ogale, F. Bai, D. Viehland, Y. Jia, D. G. Schlom, M. Wuttig, A. Roytburd and R. Ramesh, *Science*, 2004, **303**, 661.
7   M. Fan, B. Zhang, H. Wang, J. Jian, X. Sun, J. Huang, L. Li, X. Zhang and H. Wang, *Adv. Mater.*, 2017, **29**, 1606861.
8   A. Chen, Z. Bi, C.-F. Tsai, J. Lee, Q. Su, X. Zhang, Q. Jia, J. L. MacManus-Driscoll and H. Wang, *Adv. Funct. Mater.*, 2011, **21**, 2423.
9   Y. H. Hsieh, J. M. Liou, B. C. Huang, C. W. Liang, Q. He, Q. Zhan, Y. P. Chiu, Y. C. Chen and Y. H. Chu, *Adv. Mater.*, 2012, **24**, 4564.
10 S. Lee, A. Sangle, P. Lu, A. Chen, W. Zhang, J. S. Lee, H. Wang, Q. Jia and J. L. MacManus-Driscoll, *Adv. Mater.*, 2014, **26**, 6284.
11 J. L. MacManus-Driscoll, P. Zerrer, H. Wang, H. Yang, J. Yoon, A. Fouchet, R. Yu, M.G. Blamire and Q. Jia, *Nat. Mater.*, 2008, **7**, 314.
12 H. J. Liu, L. Y. Chen, Q. He , C. W. Liang, Y. Z. Chen, Y. S. Chien, Y. H. Hsieh, S. J. Lin, E. Arenholz, C. W. Luo, Y. L. Chueh, Y. C. Chen and Y. H. Chu, *ACS Nano*, 2012, **6**, 6952.
13 S. Park, Y. Horibe, T. Asada, L. S. Wielunski, N. Lee, P. L. Bonanno, S. M. O'Malley, A. A. Sirenko, A. Kazimirov, M. Tanimura, T. Gustafsson and S. W. Cheong, *Nano Lett.*, 2008, **8**, 720.
14 H. M. Zheng, F. Straub, Q. Zhan, P. L. Yang, W. K. Hsieh, F. Zavaliche, Y. H. Chu, U. Dahmen and R. Ramesh, *Adv. Mater.*, 2006, **18**, 2747.
15 J. Huang, X. Wang, N. L. Hogan, S. Wu, P. Lu, Z. Fan, Y. Dai, B Zeng, R. Starko-Bowes, J. Jian, H. Wang, L. Li, R. Prasankumar, D. Yarotski, M. Sheldon, H. Chen, Z. Jacob, X. Zhang and H. Wang, *Adv. Sci.*, 2018, 1800416.
16 A. Goyal, S. Kang, K. J. Leonard, P. M. Martin, A. A. Gapud, M. Varela, M. Paranthaman, A. O. Ijaduola, E. D. Specht, J. R. Thompson, D. K. Christen, S. J. Pennycook and F. A. List, *Supercond. Sci. Technol.*, 2005, **18**, 1533.
17 J. Yao, Z. W. Liu, Y. M. Liu, Y. Wang, C. Sun, G. Bartal, A. M. Stacy and X. Zhang, *Science*, 2008, **321(5891)**, 930.
18 A. V. Kabashin, P. Evans, S. Pastkovsky, W. Hendren, G. A. Wurtz, R. Atkinson, R. Pollard, V. A. Podolskiy, A. V. Zayats, *Nature Mater.*, 2009, **8**, 867.
19 J. K. Gansel, M. Thiel, M. S. Rill, M. Decker, K. Bade, V. Saile, G. von Freymann, S. Linden and M. Wegener, *Science*, 2009, **325(5947)**, 1513.
20 N. A. Melosh, A. Boukai, F. Diana, B. Gerardot, A. Badolato, P. M. Petroff and J. R. Heath, *Science*, 2003, **300**, 112-115.
21 N. A. Melosh, A. Boukai, F. Diana, B. Gerardot, A. Badolato, P. M. Petroff, J. R. Heath, *Science*, 2003, **300(5616)**, 112.
22 J. Huang, L.Li, P. Lu, Z. Qi, X. Sun, X. Zhang and H. Wang, *Nanoscale*, 2017, **9**, 7970.
23 L. Li, L. Sun, J. S. Gomez-Diaz, N. L. Hogan, P. Lu, F. Khatkhatay, W. Zhang, J. Jian, J. Huang, Q. Su, M. Fan, C. Jacob, J. Li, X. Zhang, Q. Jia, M. Sheldon, A. Alú, X. Li and H. Wang, *Nano Lett.*, 2016, **16**, 3936-3943.
24 J. Gao, X. Wu, Q. Li, S. Du, F. Huang, L. Liang, H. Zhang, F. Zhuge, H. Cao and Y. Song, *Adv. Mater.*, 2017, **29**, 1605324
25 J. Huang, L. Chen, J. Jian, K. Tyler, L. Li, H. Wang and H. Wang, *J. Phys.: Condens. Matter*, 2016, **28**, 025702.
26 J. Huang, M. Fan, H. Wang, L. Chen, C. Tsai, L. Li and H. Wang, *Ceram. Int.*, 2016, **42**, 12202.
27 C. Tsai, J. Huang, J. Lee, F. Khatkhatay, L. Chen, A. Chen, Q. Su and H. Wang, *Physica C*, 2015, **510**, 13.
28 J. Huang, C. Tsai, L. Chen, J. Jian, F. Khatkhatay, K. Yu and H. Wang, *J. Appl. Phys.*, 2014, **115**, 123902.
29 J. Huang and H. Wang, *Supercond. Sci. Technol.*, 2017, **30**, 114004.
30 S. Manna, J. W. Kim, M. V. Lubarda, J. Wingert, R. Harder, F. Spada, V. Lomakin, O. Shpyrko and E. E. Fullerton, *AIP Advances*, 2017, **7**, 125025.
31 J. Narayan and B. C. Larson, *J. Appl. Phys.*, 2003, **93**, 278-285.
32 L. Vitos, A. V. Ruban, H. L. Skriver and J. Kollar, *Surface Science*, 1998, **411**, 186-202.
33 S. Hayun, S. V. Ushakov and A. Navrotsky, *J. Am. Ceram. Soc.*, 2011, **94**, 3679-3682.
34 B. Meyer, J. Padilla and D. Vanderbilt, *Faraday Discuss.*, 1999, **114 (0)**, 395-405.

35   S. Okamoto, R. Goto, N. Kikuchi, O. Kitakami, T. Akiya, H. Sepehri-Amin, T. Ohkubo, K. Hono, K. Hioki and A. Hattori, *J. Appl. Phys.*, 2015, **118**, 223903.

36   Y. Zhang, X. Li, J. Jing, X. Zhang and Y. Zhao, *Journal of Magnetism and Magnetic Materials*, 2016, **408**, 228-232.

37   J. H. Hwang, V. P. Dravid, M. H. Teng, J. J. Host, B. R. Elliott, D. L. Johnson and T. O. Mason, *J. Mater. Res.*, 1997, **12**, 1076-1082.

38   J. Huang, C. Tsai, L. Chen, J. Jian, K. Yu, W. Zhang and H. Wang, 2015, *IEEE Trans. Appl. Supercond.*, **25 (3)**, 7500404.

39   J. Huang, L. Li, X. Wang, Z. Qi, M. A. P. Sebastian, T. J. Haugan and H. Wang, 2017 *IEEE Trans. Appl. Supercond.*, **27 (4)**, 8000305.

40   N. W. Kwak and W. C. Jung, *Acta Mater.*, 2016, **108**, 271-278.

41   K. Pogorzelec-Glaser, A. Rachocki, P. Ławniczak, A. Łapiński and J. Tritt-Goc, *Solid State Ionics*, 2012, **227**, 96-101.